Potentialities and Limitations of Mixing Simulations

A. Souvaliotis, S. C. Jana, and J. M. Ottino
Dept. of Chemical Engineering, R. R. McCormick School of Engineering and Applied Science,
Northwestern University, Evanston, IL 60208

As numerical simulations in mixing become pervasive, an analysis of errors becomes crucial. Purposely discretized examples with exact analytical solutions provide a reference point from which to judge the soundness of numerical solutions. Three types of errors are identified and examined: discretization, time integration, and round-off, with emphasis on the first two. Theoretical derivations and numerical examples for 2-D, steady (regular) and time-periodic (chaotic) flows indicate that errors, in general, behave as material lines. In regular flows, their magnitude increases, on the average, with at most t^2, while in chaotic flows it increases exponentially. Errors tend to align with the direction of the streamlines in regular flows and with manifolds in chaotic flows. As a result, even though exact and calculated trajectories diverge exponentially fast in chaotic flows, overall mixing patterns are reproduced, at least qualitatively, even when the velocity field is calculated using coarse meshes. For example, approximate velocity fields do reproduce qualitatively the main features of a line as it is deformed by the flow, although the error in its length may be more than 100%. It is concluded that accurate quantitative information, such as the location of periodic points or the length of a deformed line, can be obtained from numerical simulations. However, robust application of standard numerical analysis tools, such as mesh refinement, is necessary, which, in turn, can lead to nearly prohibitive computational costs.

Introduction

Theoretical investigations of mixing, particularly those involving complex flow domains and time-dependent flows, increasingly rely on numerical simulations (Tjahjadi and Ottino, 1991; Jana and Ottino, 1992; Tanguy et al., 1992; Avalosse et al., 1992; Niederkorn and Ottino, 1993). This trend has been facilitated by the availability of powerful computers and the existence of commercial flow-simulation packages. From a numerical point of view, both the solution of the fluid mechanics problem, that is, obtaining $u(x,t)$, and the integration of

$$\frac{dx}{dt} = u(x;t), \qquad \nabla \cdot u = 0 \tag{1}$$

are challenging. (The equation of continuity, $\nabla \cdot u = 0$, implies that the study is confined to incompressible fluids and that Eq. 1 represents a conservative dynamical system.) In the majority of flows of interests, the geometry is three-dimensional, complex and, often, time varying. The numerical solution of this class of problems requires significant amounts of both computational time and memory. Moreover, the recent shift toward chaotic mixing has further increased the computational load (Ottino, 1989). The computational time spent in the integration of Eq. 1 and the memory required for the faithful representation of the deformation of a material line can be enormous (Franjione and Ottino, 1987).

There are three types of error present in mixing simulations: *discretization* (or approximation), *time integration*, and *round-off* errors. The numerical velocity field is only an approximation of the actual velocity field. In fact, Eq. 1 can be written as

---

Correspondence concerning this article should be addressed to J. M. Ottino.
Present address of S. C. Jana, GE CRD, P.O. Box 8, Schenectady, NY 12301.

$$\frac{dx}{dt} = u(x;t) + \epsilon u^*(x;t), \tag{2}$$

where ϵu^* represents a perturbation of the exact velocity field, associated with the discretization error. The parameter ϵ is a function of the characteristic grid size, Δx_G. In many cases (such as finite elements, finite differences) ϵ is $O(\Delta x_G^k)$, where k is a small integer.

It is known that chaotic flows are sensitive to small perturbations. For example, Niederkorn and Ottino (1993) examined the mixing of viscoelastic fluids within a journal bearing. Although the changes in the velocity field, as compared to the Newtonian case, were of the order of a few percent only, the mixing patterns were significantly different. A relevant question then is whether or not the theoretically predicted mixing patterns are significantly affected by perturbations of the velocity field due to numerical approximations.

The second type of error originates from the numerical integration of Eq. 1. This type of error depends on the time step and the integration scheme and is present even when the velocity field is known analytically. Numerical integration schemes introduce nonlinearities that do not exist in the original problem (Yee et al., 1991), and may therefore fail to capture the correct long-time dynamics by altering or even destroying the Hamiltonian nature of the governing set of equations due to accumulated errors. This observation has motivated the development of symplectic integrators (for example, Channell and Scovel, 1990; Candy and Rozmus, 1991; references therein). These issues notwithstanding, in mixing simulations we are primarily interested in short- to intermediate-time behavior. As will be discussed in a later section, the use of adaptive time steps and high-order schemes can effectively eliminate errors associated with time integration.

The final source of error is the finite accuracy of any machine, which appears in the calculations as round-off error. In general, round-off error is orders of magnitude lower than the discretization and the time integration error. However, due to the exponential stretching present in chaotic flows, even this otherwise insignificant error grows to measurable levels within a short time. For example, if the length of the line is doubled every time period, T, then a perturbation of 10^{-16} grows to 1 after $53.2T$. Although an increase of the length of a material line of the order of 10^{16} implies a reduction of the striation thickness of the same order and, presumably, a more than satisfactory level of mixing, it also demonstrates the pitfalls of chaotic advection simulations.

The main objective of this article is to put into evidence possible limitations of numerically supported mixing studies and to document the results by means of key examples. Particular emphasis is placed on how the discretization error of the velocity field manifests itself in the various dynamical tools used in studying chaotic advection. The time-periodic journal-bearing flow is used as our primary example. The chaotic mixing patterns of this flow have been analyzed extensively both theoretically and experimentally (Swanson and Ottino, 1990). An attractive feature of this flow is that the velocity field is known analytically (Wannier, 1950), which allows for a direct evaluation of the discretization error.

The approximation methods employed in our study are the boundary integral equation method (BIEM) and an approximation method reminiscent of first-order finite elements, referred in the following as *pseudo-finite-element method* (PFEM). It is not our purpose to comparatively evaluate these techniques, although relevant comments will be made occasionally. Instead, we seek to detect generic symptoms of approximation errors in the mixing patterns, irrespective of the particular numerical technique in use.

It has to be emphasized that, in the numerical examples presented in this article, we have intentionally used coarse grids to magnify the numerical errors and mimic the approximations in more realistic problems. The journal-bearing flow is two-dimensional and steady, the governing equations are linear, and the flow domain is smooth. Therefore, very accurate solutions, say, $O(10^{-5})$ or less, can be obtained with virtually any numerical scheme, and with relatively minimal computational resources. However, most mixing problems of practical importance involve complicated, three-dimensional flow domains and time-dependent flows, and higher approximation errors are inevitable.

The remainder of this article is organized as follows: a short summary of mixing theory appears in the following section; the next sections describe various computational errors and their effect on mixing patterns using model flow problems.

Background

The theoretical foundations of mixing are based on kinematical relations describing the movement and deformation of material lines and surfaces within a given flow field. Here, we present a summary of mixing theory (Ottino, 1989) as a background for the discussion in the following sections and to introduce the reader to the notation and formalism to be used in the remainder of the article.

Integration of Eq. 1 between time t and $t+\Delta t$ results in the mapping function, f, so that

$$x = f(X, \Delta t; t, \kappa, \epsilon), \tag{3}$$

signifying that the particle located at X in time t will be found at x in $t+\Delta t$. In our notation, κ is a symbolic representation of the set of geometrical and flow parameters, and ϵ represents deviations due to numerical inaccuracies (Eq. 2). For steady flows, f does not depend explicitly on t. For periodic flows, where a period T can be defined, a natural definition of the mapping is

$$x^n = f^n(x^0), \tag{4}$$

where $x^n = x(nT)$, so that n successive applications of the mapping f take a fluid particle from x^0 to x^n. The evolution of a differential material line, dX, between t and $t+\Delta t$ is described by

$$dx = F \cdot dX, \tag{5}$$

with F being the deformation gradient tensor, $\|\partial x_i/\partial X_j\|$. Alternatively, F can be defined as the Jacobian of f. Occasionally, the notation

$$F^{(t\to t')} = F(X, t'-t; t, \kappa) \tag{6}$$

will be used in order to distinguish among successive applications of a general mapping f, on the same particle, originally at $X = X(0)$. In this case, $F^{(t\rightarrow t')}$ is the Jacobian of the mapping representing the motion of the particle X, between t and t'.

The periodic points of f^n (Eq. 4), that is, points P such that $P = f^n(P)$, are central to the understanding of chaotic mixing. A fixed point is a point that does not move, while an order n periodic point is a point that returns to its original position after n periods. Fixed and periodic points are characterized as hyperbolic and elliptic according to the eigenvalues, l, of the Jacobian of f^n. In two-dimensional flows, if the eigenvalues are imaginary, the point is elliptic. If they are real, the point is hyperbolic. Elliptic and hyperbolic points have different effects on mixing. Neighboring material circulates around elliptic points, whereas material is stretched in one direction and contracted in another near hyperbolic points. Since stretching is beneficial to mixing, hyperbolic points are desirable in mixing flows.

A hyperbolic point, P, is associated with two manifolds, representing the trajectories along which a particle is attracted to (stable manifold) and moves away from (unstable manifold) P. In steady, bounded, two-dimensional flows, a manifold that originates from a hyperbolic point ends either on the same or on another hyperbolic point. Consequently, the material that is attracted toward P in order to be stretched comes from confined regions of the flow domain. This is an alternative qualitative explanation of the limited mixing capabilities of these kinds of flows. If, on the other hand, the stable manifold of P intersects with a manifold of another hyperbolic point, new material is continuously attracted toward P. The result is a repetitive stretching and folding that gives rise to chaotic dynamics.

Model Mixing Problems and Numerical Approximation

In this section the model flow problems and the numerical techniques used in this investigation are described.

The flow between concentric cylinders will be used to demonstrate the effect of numerical time integration on particle trajectories. Both the velocity field and the corresponding fluid particle trajectories (and the mapping function f) are known analytically. In addition, the pure shear flow kinematics permit a straightforward interpretation of the findings.

The second model mixing flow is the time-periodic Stokes flow between two eccentric cylinders (journal bearing). This flow has been extensively analyzed (Chaiken et al., 1986; Swanson and Ottino, 1990; Tjahjadi and Ottino, 1991). Excellent agreement between the experimentally observed and the theoretically predicted mixing patterns has been demonstrated (Swanson and Ottino, 1990), the latter being based on an analytically known flow field (Wannier, 1950). The existence of an analytical velocity field makes this flow an ideal test case for the examination of the effects of the discretization errors in mixing simulations.

Flow between concentric cylinders

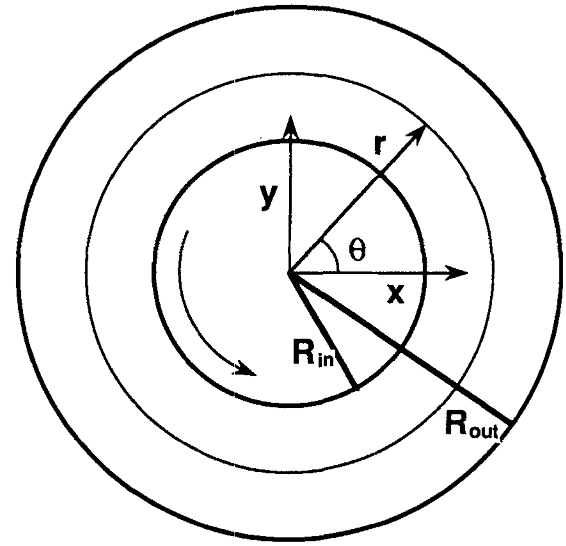

Figure 1. Concentric cylinder geometry.

The concentric cylinder geometry is shown in Figure 1. The two cylinders can rotate independently, but in this study steady motion of the inner cylinder is assumed, while the outer cylinder is stationary. The angular velocity in dimensionless form is

$$u_\theta(r) = \frac{1}{r^2}\frac{r^2-(\mu+1)^2}{1-(\mu+1)^2}, \tag{7}$$

where r is the dimensionless radial position with R_{in} as the characteristic length and $1/\Omega$ the characteristic time, Ω being the angular velocity, and $\mu = R_{\text{out}}/R_{\text{in}} - 1$ (in analogy with the eccentric cylinders problem).

For this flow, the particle locations are known analytically. If the initial position of a particle is (r_0, θ_0), its location at time t is $[r_0, \theta_0 + u_\theta(r_0)t]$. The same calculation is *error free* in cylindrical coordinates, irrespective of the numerical integration scheme, because the streamlines coincide with the coordinate lines and the velocity is constant. In order to introduce numerical errors, we purposely carry out the numerical integrations in a Cartesian coordinate system. In this system

$$u_x = r u_\theta(r)\sin\theta; \qquad u_y = r u_\theta(r)\cos\theta. \tag{8}$$

Flow between eccentric cylinders

The journal-bearing geometry is presented in Figure 2. The flow domain is confined between two cylinders with parallel axes that do not coincide. The radii of the inner and outer cylinder are R_{in} and R_{out}, respectively. The flow domain is completely specified by two dimensionless parameters, the dimensionless gap, $\mu = (R_{\text{out}}/R_{\text{in}}) - 1$, and the eccentricity, $e = d/(R_{\text{out}} - R_{\text{in}})$, with d being the distance between the centers of the two cylinders. The flow domain can be transformed to a rectangle using the bipolar coordinate system sketched in Figure 2.

The two cylinders can rotate independently. For the time-dependent Stokes flow, the streamfunction, Ψ, can be written as

$$\Psi(x,y,t) = \Psi_{\text{in}}(x,y)\Omega_{\text{in}}(t) + \Psi_{\text{out}}(x,y)\Omega_{\text{out}}(t), \tag{9}$$

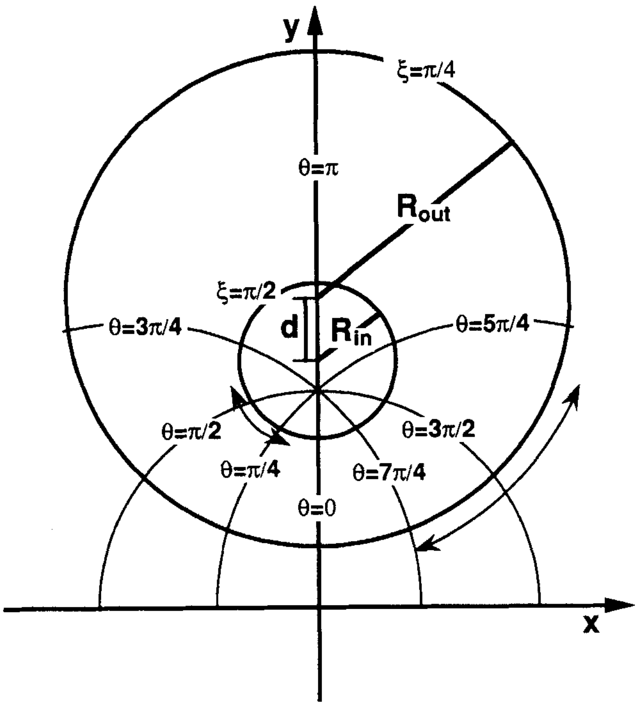

Figure 2. Eccentric cylinders geometry (journal bearing) and the bipolar coordinate system.

where Ψ_{in} and Ψ_{out} are the streamfunctions corresponding to the motion of the inner and outer cylinder, and Ω_{in} and Ω_{out} are the angular speeds of the two cylinders. The movement of the boundaries is described by periodic functions of time. Swanson (1991) examined the chaotic advection patterns emanating from various wave forms in this system. Here, we consider only the square wave, which is described as

$$\Omega_{\text{in}}(t)=\begin{cases}\Omega_{\text{in}} & 0\le t<T/4\\ 0 & T/4\le t<3T/4\\ \Omega_{\text{in}} & 3T/4\le t<T\end{cases}$$
$$\Omega_{\text{out}}(t)=\begin{cases}0 & 0\le t<T/4\\ \Omega_{\text{out}} & T/4\le t<3T/4\\ 0 & 3T/4\le t<T,\end{cases}\tag{10}$$

where T is the period of the flow. Then the protocol of movement is completely characterized by $\Omega=\Omega_{\text{in}}/\Omega_{\text{out}}$ and the total displacement, Θ, defined as

$$\Theta=\int_0^T\Omega_{\text{out}}(t)dt.\tag{11}$$

In the examples to follow, the geometrical parameters are set to $\mu=2$ and $e=0.45$. Also the ratio of the angular velocities, Ω, is set to -3, so that both the cylinders experience equal linear displacement and reveal symmetries in mixing patterns. Then, the only remaining parameter is the displacement, Θ (Eq. 11), and its value uniquely characterizes the protocol. Here, we have concentrated on the 180° and 360° protocols. In both cases, chaotic and regular regions coexist, although the second protocol results in a significantly larger chaotic region. These protocols produce relatively mild stretching. Consequently, the growth of various errors is slower and can be monitored for longer times.

Numerical approximations

The approximate velocity fields of the journal-bearing flow have been obtained using the BIEM and an approximation procedure, which will be designated as PFEM.

The velocity field in BIEM is expressed in terms of line or surface integrals involving boundary velocities and surface force distribution, and satisfies the equation of continuity everywhere in the flow domain. One advantage of this method is that the discretization of the entire fluid domain can be avoided. The unknowns, for example, surface force, appear only at the boundaries. In the boundary integral representation the velocity at a point $\boldsymbol{x}_0$ is expressed as

$$u_i(\boldsymbol{x}_0)=C\int_D[S_{ij}(\boldsymbol{x}')\phi_j(\boldsymbol{x})-T_{ijk}(\boldsymbol{x}')u_j(\boldsymbol{x})n_k(\boldsymbol{x})]dS;\quad i,j,k=x,y,\tag{12}$$

where $\boldsymbol{\phi}$ is the unknown surface force, S is the boundary of the fluid domain D, $\boldsymbol{n}$ is the unit normal pointing out of D at $\boldsymbol{x}$ on S, $\boldsymbol{x}'=\boldsymbol{x}-\boldsymbol{x}_0$, and $C=(1/4\pi\eta)$ when $\boldsymbol{x}_0$ is inside D and $(1/2\pi\eta)$ when $\boldsymbol{x}_0$ is on D with η as the viscosity. The free-space Green's function, $S_{ij}(\boldsymbol{x}')$, is given by

$$S_{ij}(\boldsymbol{x}')=\delta_{ij}\ln|\boldsymbol{x}'|-\frac{x_i'x_j'}{|\boldsymbol{x}'|^2},\tag{13}$$

with its associated stress field as

$$T_{ijk}(\boldsymbol{x}')=4\eta\frac{x_i'x_j'x_k'}{|\boldsymbol{x}'|^4}.\tag{14}$$

After discretization of the boundary S into N elements, Eq. 12 can be written as

$$u_i(\boldsymbol{x}_0)=C\sum_{n=1}^{N}\left\{\int_{S_n}[S_{ij}(\boldsymbol{x}')\phi_j(\boldsymbol{x})-T_{ijk}(\boldsymbol{x}')u_j(\boldsymbol{x})n_k(\boldsymbol{x})]dS\right\},\tag{15}$$

where S_n is the arc length of the nth boundary element; in this article we use only the straight line elements. Also $\boldsymbol{u}$ and $\boldsymbol{\phi}$ are assumed to be piecewise constant on each element, and Eq. 15 simplifies to

$$u_i(\boldsymbol{x}_0)=C\left[\sum_{n=1}^{N}A_{ij}(\boldsymbol{x}')\phi_j(\boldsymbol{x}_n)-\sum_{n=1}^{N}B_{ij}(\boldsymbol{x}')u_j(\boldsymbol{x}_n)\right],\tag{16}$$

where $\boldsymbol{x}_n$ denotes the middle of the nth element and the terms A_{ij} and B_{ij} are given as

$$A_{ij}(\boldsymbol{x}')=\int_{S_n}S_{ij}(\boldsymbol{x}')dS\tag{17a}$$

$$B_{ij}(x') = \int_{S_n} T_{ijk}(x') n_k(x) dS. \tag{17b}$$

Considering the point x_0 on S, the system of Eq. 16 is solved for ϕ from the known boundary velocities. Once the distribution of ϕ is determined, the velocity at any interior point x_0 is obtained using again Eq. 16. One advantage of using straight line elements is that the integrals in Eq. 17 can be evaluated analytically in many cases. A detailed account of various integral formulations of Eq. 12 and a discussion of errors incurred in discretization of S and approximation of ϕ and u can be found in Pozrikidis (1992).

PFEM velocity fields, on the other hand, need discretization of the entire flow domain and can be obtained as follows. An $M_1 \times M_2$ uniform grid, in bipolar coordinates, is overlaid on the flow domain, forming $(M_1 - 1) \times (M_2 - 1)$ elements. The value of the analytical velocity is assigned to every grid point and, within each element, the velocities are obtained using bilinear interpolation in the bipolar system. The approximate velocity fields, thus obtained, are second-order accurate and reminiscent of isoparametric rectangular finite-element solutions, justifying the name *pseudo*-FEM. Notice that the approximate velocities are continuous but their derivatives are not.

Evolution of Numerically Induced Errors

Time integration error

Theory. We are interested in the trajectory of a particle originally located at $x^{(0)}$, calculated using the analytical velocity field (Eq. 2, $\epsilon = 0$) and a time integration scheme. The sequence $x^{(1)}, x^{(2)}, \ldots, x^{(i-1)}, x^{(i)}, x^{(i+1)}, \ldots$, (Figure 3) denotes the exact locations of the particle after each time-step, while the sequence $x_N^{(1)}, x_N^{(2)}, \ldots, x_N^{(i-1)}, x_N^{(i)}, x_N^{(i+1)}, \ldots$, denotes the calculated trajectory. Accordingly, in order to follow the orientation and evolution of instantaneous errors one can define an *error vector*, $\Delta x^{(i)}$, such that

$$\Delta x^{(i)} = x_N^{(i)} - x^{(i)}. \tag{18}$$

Following standard numerical analysis notation, $\Delta x^{(i)}$ will be called overall or *global* error. Using Eq. 3, with $\epsilon = 0$, one can also define a *local* error, $\Delta x_N^{(i)}$, as

$$\Delta x_N^{(i)} = x_N^{(i)} - f(x_N^{(i-1)}, \Delta t_i; t_{i-1}, \kappa), \tag{19}$$

where f is the exact mapping and Δt_i the ith time step. If an $(m-1)$th-order (global accuracy) scheme is used for the numerical integration, $|\Delta x_N^{(i)}| = O(\Delta t_i^m)$.

Using the notation of Eq. 6, with i instead of t_i, we can write, up to first order,

$$f(x_N^{(i)}, \Delta t_{i+1}; t_i, \kappa) - x^{(i+1)} = F^{(i \to i+1)} \cdot (x_N^{(i)} - x^{(i)})$$

$$= F^{(i \to i+1)} \cdot \Delta x^{(i)}. \tag{20}$$

Notice that $F^{(i \to j)}$ refers to the exact velocity field. Due to Eq. 19, Eq. 20 can be rewritten as

$$\Delta x^{(i+1)} = x_N^{(i+1)} - x^{(i+1)} = F^{(i \to i+1)} \cdot \Delta x^{(i)} + \Delta x_N^{(i+1)}. \tag{21}$$

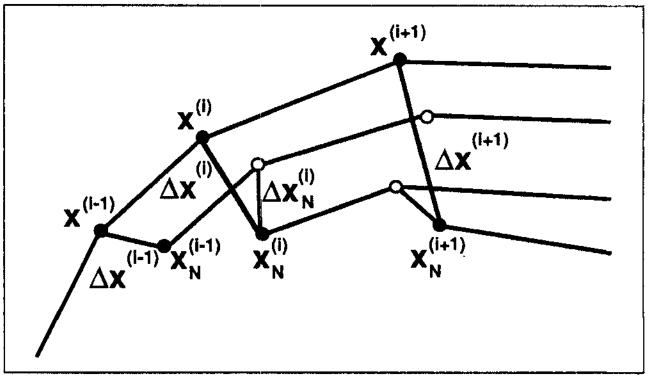

Figure 3. Analytical particle trajectory ($x^{(i-1)}$, $x^{(i)}$, $x^{(i+1)}$) and its approximation ($x_N^{(i-1)}$, $x_N^{(i)}$, $x_N^{(i+1)}$) due to time integration errors.

$\Delta x_N^{(i)}$ and $\Delta x^{(i)}$ are, respectively, the local and global errors.

One can write $F^{(i \to j)} = F^{(k \to j)} \cdot F^{(i \to k)}$. In this case, the global error at the kth time step is

$$\Delta x^{(k)} = F^{(1 \to k)} \cdot \Delta x_N^{(1)} + F^{(2 \to k)} \cdot \Delta x_N^{(2)} + \ldots + \Delta x_N^{(k)}$$

$$= \sum_{i=1}^{k} F^{(i \to k)} \cdot \Delta x_N^{(i)}. \tag{22}$$

The local error, $\Delta x_N^{(i)}$, behaves as a material line, with its deformation controlled by a relation similar to Eq. 5. For example, in a steady, two-dimensional and bounded flow, the length of a material line is, asymptotically, proportional to t (Ottino, 1989). If Δt is constant, the length of $\Delta x_N^{(i)}$ at time $k\Delta t$ is

$$|\Delta x_N^{(i)}(k\Delta t)| \equiv |F^{(i \to k)} \cdot \Delta x_N^{(i)}| \approx C_i (k-i) \Delta t |\Delta x_N^{(i)}|, \tag{23}$$

where C_i is positive and depends on the kinematics and the initial orientation of $\Delta x_N^{(i)}$ with respect to the streamlines. The total error at time $t = k\Delta t$ is

$$|\Delta x^{(k)}| = \left| \sum_{i=1}^{k} F^{(i \to k)} \cdot \Delta x_N^{(i)} \right| \leq \sum_{i=1}^{k} |F^{(i \to k)} \cdot \Delta x_N^{(i)}|$$

$$\approx \sum_{i=1}^{k} C_i (k-i) \Delta t |\Delta x_N^{(i)}|. \tag{24}$$

If $C = \max(C_i)$, $|\Delta x_N| = \max|\Delta x_N^{(i)}|$, and strict equality is assumed in Eq. 24, then

$$|\Delta x^{(k)}| \leq C\Delta t |\Delta x_N| \sum_{i=1}^{k} (k-i) = C\Delta t |\Delta x_N| \frac{k(k-1)}{2}$$

$$< \frac{C}{2} \frac{|\Delta x_N|}{\Delta t} (k\Delta t)^2. \tag{25}$$

Equation 25 suggests that the global error is proportional to t^2. Furthermore, since $|\Delta x_N| = C_N (\Delta t)^m$, we can write

$$|\Delta x^{(k)}| < \frac{C}{2}\frac{C_N \Delta t^m}{\Delta t}t^2 = \frac{CC_N}{2}\Delta t^{m-1}t^2. \tag{26}$$

It should be noted that Eq. 23 is valid only in an average sense, as time increases. In fact, for short times, the length of a material line may decrease. The special case of $\Delta x_N^{(i)}$ being parallel to the flow will be discussed in the following section.

A relation similar to Eq. 26 can be derived for the evolution of the round-off error, with $|\Delta x_R|$ being the precision of the computational device. In general, this type of error is expected to be negligible, several orders of magnitude smaller than the time integration, or the approximation error. Yet, one should be aware that this error imposes a limit on the accuracy of any time integration scheme, and consequently, to the lower value of time step that can be used.

Flow between Concentric Cylinders. Consider now the implications of the preceding results on the flow between two concentric cylinders (Figure 1). The exact locations of fluid particles are compared to calculated ones, according to three explicit time integration methods with constant time steps. The methods and their corresponding formulas are:

(a) First-order Euler scheme

$$x^{(j+1)} = x^{(j)} + \Delta t u^{(j)}. \tag{27}$$

(b) Second-order Adams multistep method

$$x^{(j+1)} = x^{(j)} + \frac{\Delta t}{2}(3u^{(j)} - u^{(j-1)}). \tag{28}$$

(c) Third-order Adams multistep method

$$x^{(j+1)} = x^{(j)} + \frac{\Delta t}{12}(23u^{(j)} - 16u^{(j-1)} + 5u^{(j-2)}). \tag{29}$$

Note that there is no particular reason in choosing explicit time integration techniques apart from their simplicity. However, values of Δt used in all computations are sufficiently small so as to guarantee stability of such explicit schemes.

The movement of a particle placed at $r_0 = 1 + (\mu + 1)/2$, $\theta_0 = 0$ is calculated using various time steps for $\mu = 0.5$. The error is defined as

$$|\Delta x(t)| = \sqrt{[x(t) - r_0\cos(u_\theta(r)t)]^2 + [y(t) - r_0\sin(u_\theta(r)t)]^2}, \tag{30}$$

where $x(t)$ and $y(t)$ are the calculated coordinates.

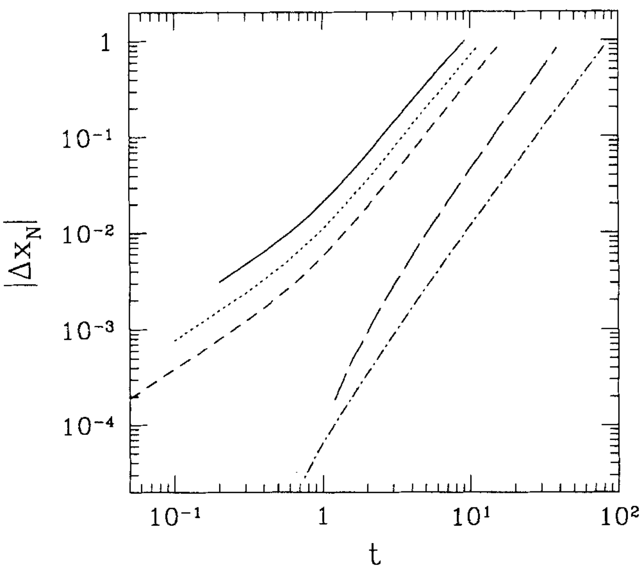

Figure 4. Global error (Eq. 26) due to numerical time integration as a function of time, for the concentric cylinder flow ($\mu = 0.5$) and initial location at $r = 1 + (\mu + 1)/2$.

(——) Euler, $\Delta t = 0.2$; (····) Euler, $\Delta t = 0.1$; (– – –) Euler, $\Delta t = 0.05$; (— —) Adams 3rd order, $\Delta t = 0.4$; (–··–) Adams 3rd order, $\Delta t = 0.25$.

In Figure 4, the error is plotted as a function of time, for $\Delta t = 0.2$, 0.1, and 0.05 (for the Euler scheme) and 0.4 and 0.25 (for the third-order scheme). The slopes of the lines for $t > 1$ are close to 2, as predicted by Eq. 26. Initially, the error of the Euler integration is proportional to t, an indication of error growth through simple addition. For both methods, the global error in the quadratic regime is, as predicted, $O(\Delta t)$ and $O(\Delta t^3)$. In addition, Figure 4 clearly demonstrates that the first-order Euler scheme is an unreliable method for the particle tracking within a flow field. The arclength error at $t = 10$ is 15%, and 8.9% for $\Delta t = 0.1$ and $\Delta t = 0.05$. Notice that at $t = 10$, the inner cylinder has not even completed two revolutions.

Figure 5 shows results corresponding to the second- and third-order methods. Although after long times the error increases with t^2 in both cases, the second-order method pro-

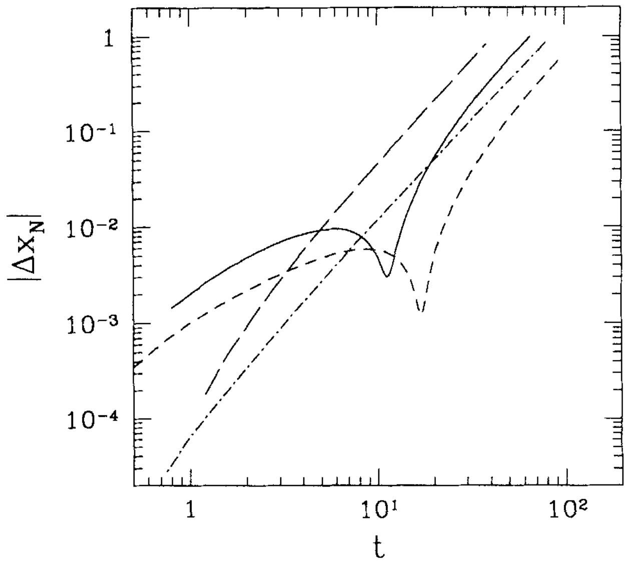

Figure 5. Global error (Eq. 26) due to numerical time integration as a function of time, for the concentric cylinder flow ($\mu = 0.5$) and initial location at $r = 1 + (\mu + 1)/2$.

(——) Adams 2nd order, $\Delta t = 0.4$; (····) Adams 2nd order, $\Delta t = 0.25$; (– – –) Adams 3rd order, $\Delta t = 0.4$; (— —) Adams 3rd order, $\Delta t = 0.25$.

duces more accurate results. Furthermore, the error of the second-order method decreases, before reaching the quadratic regime.

This counterintuitive result is a consequence of the flow kinematics and can be rationalized as follows. Although the local error is indeed third and fourth order, respectively, its orientation plays an interesting role. It turns out that in the first-order Euler and the third-order Adams method, the local error, $\Delta x_N^{(i)}$, is perpendicular to the streamlines, while in the second-order Adams method it is parallel to the leading term in Δt. Specifically, for a particle at (x, y) or, equivalently, at (r, θ) the components of the local error are

$$\Delta x = \frac{[u_\theta(r)]^2 \Delta t^2}{2} r \cos\theta + \text{h.o.t.};$$

$$\Delta y = \frac{[u_\theta(r)]^2 \Delta t^2}{2} r \sin\theta + \text{h.o.t.} \tag{31}$$

for the Euler method and

$$\Delta x = \frac{5}{12}[u_\theta(r)]^3 \Delta t^3 r \sin\theta + \text{h.o.t.};$$

$$\Delta y = -\frac{5}{12}[u_\theta(r)]^3 \Delta t^3 r \cos\theta + \text{h.o.t.} \tag{32}$$

for the second-order method. The preceding estimates have been obtained assuming that the exact (analytical) location is known at all previous t's. In a shear flow, such as the one under consideration here, the length of a material line does not increase if the line is oriented parallel to the local flow. Therefore, the overall error of the second-order method for short times is simply equal to the sum of the local errors. Moreover, since $\Delta x_N^{(i)}$ points upstream (Eq. 32), its length initially decreases. This phenomenon is responsible for the minima in Figure 5. In general, $\Delta x_N^{(i)}$ is not exactly parallel to the streamlines due to the higher-order terms and, eventually, at long times, its length will increase.

Equations 31 and 32 are mathematically exact only in the limited case of simple shear flow. A qualitatively similar effect can be observed in other two-dimensional, steady, and bounded flows (such as, journal bearing), especially in regions with predominantly shear kinematics. The preceding discussion illustrates the effect of the *orientation*, in addition to the magnitude, of the local error in the accumulated error.

Discretization error

In most cases of practical interest, an analytical velocity field is not available. Instead, an approximate velocity field is obtained through direct numerical simulations. Furthermore, in collocation schemes, the velocity is only known at a finite number of points (grid points). Inevitably, the calculated trajectories are also approximate. Errors originate from both the *discretization* of the system of PDEs and the *interpolation* within grid elements (collocation schemes). In general, the error from both sources is a function of a characteristic gridsize, Δx_G, but not necessarily similar. Yet, the accuracy of the interpolation is always limited by the accuracy of the discretized data. Nevertheless, there exists an interpolation relation *consistent* with the numerical scheme, that is, one that has the same order of error with the discretization scheme. For example, in finite-element methods it is assumed that the velocity field can be expressed, within every element, as a polynomial. A consistent interpolation scheme uses the same polynomial. For linear elements, the discretization error is $O(\Delta x_G^2)$, which is also the order of error of the bilinear interpolation. There is a consistent polynomial interpolation scheme for finite difference (collocation) schemes as well. For central finite differences, the approximation error is $O(\Delta x_G^2)$, suggesting a bilinear interpolation scheme, whereas higher-order schemes require a higher-order interpolation. In BIEM, the velocity field at any point of the flow domain is uniquely determined in terms of the boundary values of point forces or dipoles without the need of interpolation. Finally, in spectral and pseudospectral methods, it is implicitly assumed that the solution can be globally represented by a high-order polynomial. In the remainder of this article we will not distinguish between the two errors, assuming that the interpolation is always consistent with the discretization.

A major concern in numerical approximations is that the continuity constraint, $\nabla \cdot \boldsymbol{u} = 0$, in Eq. 1, may not be satisfied uniformly. This is the case with many domain discretization schemes using the primary variables (velocity, pressure) formulation. When this happens, the Hamiltonian nature of the governing system of equations is violated. A definite sign of this behavior is occurrence of streamlines that do not close. Notice that the integral equations in BIEM automatically satisfy the continuity equation and preserve the Hamiltonian character. Even in the cases of numerically evaluated integrals in Eq. 17, the calculated velocity field will be divergence free and streamlines will close.

Consider Eq. 1, where the velocity has been obtained by a numerical procedure or, in general, it is only an approximation of the exact one ($\epsilon \neq 0$ in Eq. 2). Assume also that the time integration error is negligible. The notation of Eqs. 18–19 is used, with the symbol N substituted by D to indicate discretization errors. Similar to Eq. 21, one can write

$$\Delta \boldsymbol{x}^{(i+1)} = \boldsymbol{F}^{(i\rightarrow i+1)} \cdot \Delta \boldsymbol{x}^{(i)} + \epsilon \frac{\partial f}{\partial \epsilon} = \boldsymbol{F}^{(i\rightarrow i+1)} \cdot \Delta \boldsymbol{x}^{(i)} + \Delta \boldsymbol{x}_D^{(i)}. \tag{33}$$

The local error, $\Delta \boldsymbol{x}_D^{(i)}$, can be estimated using a Taylor series expansion of Eq. 3 in time for the mapping, f, as

$$f(\boldsymbol{x}, \Delta t; \epsilon) = \boldsymbol{x} + \Delta t[\boldsymbol{u}(\boldsymbol{x}) + \epsilon \boldsymbol{u}^*] + O(\Delta t^2). \tag{34}$$

Then,

$$\Delta \boldsymbol{x}_D^{(i)} = \epsilon \frac{\partial f}{\partial \epsilon} = \epsilon \Delta t \boldsymbol{u}^*. \tag{35}$$

Starting with Eq. 33, much of the analysis presented for the time integration error can be repeated, using $\Delta \boldsymbol{x}_D^{(i)}$ instead of $\Delta \boldsymbol{x}_N^{(i)}$. For example, the error in a steady, two-dimensional, bounded flow becomes

$$|\Delta \boldsymbol{x}^{(k)}| < \frac{C}{2} \frac{|\Delta \boldsymbol{x}_D|}{\Delta t} t^2 = \frac{C}{2} \epsilon |\boldsymbol{u}^*| t^2. \tag{36}$$

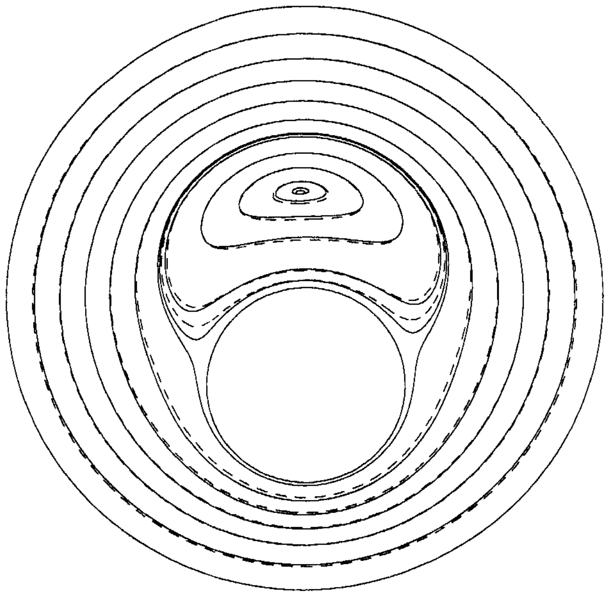

Figure 6. Representative streamlines for the journal bearing ($\mu = 2$, $e = 0.45$) flow with the outer cylinder rotating.

(——) analytical and (— —) 11×21 PFEM velocity field.

The mechanism responsible for the second-order time dependence in Eq. 36 is the "drifting" of the particle to neighboring *exact* streamlines, resulting in calculated particle trajectories that do not close, even for steady, two-dimensional flows. Whenever the approximate velocity field results in closed trajectories, the global error is, on the average, proportional to time.

Figure 6 shows the streamline portrait of the journal-bearing flow with the outer cylinder rotating. Continuous lines correspond to streamlines calculated with the analytical velocity, while dashed lines correspond to streamlines obtained from the very coarse 11×21 PFEM field. The maximum error for this velocity field (Euclidean norm) is 0.048, when the maximum velocity magnitude is 1. The average error is 0.0047 (one order of magnitude less than the maximum error). This value was calculated using up to 10^5 uniformly distributed points and is independent from the number of sample points for sample sizes larger than 10^4. For the 21×41 grid, the errors are 0.012 and 0.0017, consistent with the expected second-order convergence. The maximum and average error values in the velocity field calculated by BIEM are, respectively, 0.002 and 0.0004 using, respectively, 120 and 40 elements on the outer and inner cylinders.

Despite the coarse grid, the differences in the streamlines of Figure 6 are hardly discernible, except in the neighborhood of the separation line. In addition, the approximate solutions produced closed streamlines. In fact, it can be shown that, for symmetric velocity fields and symmetric grids, the calculated trajectories always close, irrespective of the approximation error (Appendix), even when the continuity constrain is not satisfied. Consequently, the error normal to the streamlines is a periodic function of time and remains bounded. However, this is not everything that matters.

An important issue is errors in circulation time, that is, the time taken by a point to traverse a closed streamline once. Such errors are difficult to detect, especially if a judgment of the quality of the results is based on visual inspection of the calculated streamlines, as is the standard practice. Even when a discretized velocity field results in closed streamlines, the error along the direction of the streamlines is crucial, especially as time advances, since the overall effect of a flow is to align any material line, and, consequently, the error, with them.

The error along and normal to the streamlines is presented in Figure 7 for some representative trajectories of Figure 6. The calculations were based on grids of the form $M \times (2M)$. The tracer particles were originally placed along the symmetry line and were followed until they crossed this line again, having completed half of their circulatory trajectory. The time

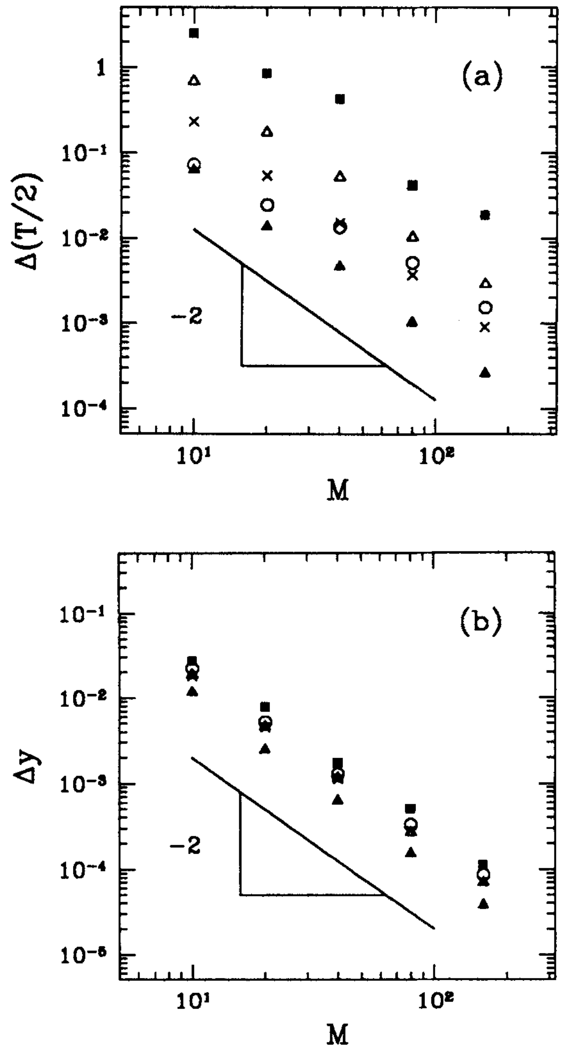

Figure 7. Steady journal bearing flow ($\mu = 2$, $e = 0.45$) with the outer cylinder rotating: Errors due to velocity approximations (PFEM velocity fields of the form $M \times 2M$) as a function of M, for representative trajectories originating from the symmetry line.

Error in (a) half of the circulation time, $\Delta(T/2)$, and (b) the location of the second intersection with the symmetry line. The symbols represent different initial conditions taken on the symmetry line.

required for this motion, representing half the circulation time, and the y-coordinate where the trajectories cross the symmetry line are compared to the ones obtained by the analytical velocity. The errors in half the circulation time and in the y-coordinate crossings are plotted in Figure 7 (a and b, respectively). In both cases, the error scales with $1/M^2$ and is proportional to the error in the approximate velocity field, as predicted by Eq. 36. Some deviations from this behavior were observed for the circulation times calculated from the coarser grids and are, most probably, associated with the higher-order discontinuities in the velocity field. In order to compare the magnitude of the two types of error, the difference in the circulation time was translated into length by multiplying with the average velocity along each trajectory. Except for the innermost streamlines of the recirculation area, the corresponding "lengths" were more than two times the error in the y-coordinate.

At this point it should be reiterated that the streamlines of Figure 6 have been calculated by integrating Eq. 1. Alternatively, streamlines can be obtained by solving

$$\nabla^2\Psi = \frac{\partial u_x}{\partial y} - \frac{\partial u_y}{\partial x}, \tag{37}$$

along with appropriate boundary conditions for the streamfunction, Ψ. Contours of constant Ψ can be used for representing the streamlines of the flow. The righthand side of Eq. 37 can be evaluated using numerical differentiation. Since Ψ is a scalar field, the resulting streamlines always close. In addition, the Laplace operator is an effective smoothing operator. This method is advantageous in those studies intended to reveal the topology of the flow, but we believe that it is not suitable for mixing simulations. One particular problem is that the smoothing masks the inaccuracies of the velocity field. In addition, information regarding circulation times cannot be obtained easily.

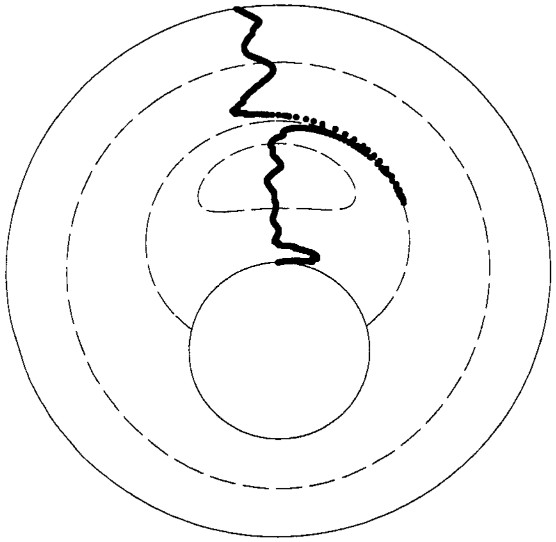

Figure 8. Steady journal bearing flow ($\mu=2$, e$=0.45$): Location of particles originally placed on the symmetry line and advected forward by the 11 $\times$21 PFEM field (for two revolutions of the outer cylinder) and backward by the analytical field (for equal time).

An alternative test of the accuracy of the particle tracking scheme is presented in Figure 8. A number of tracers are advected for some time by an approximate field, in this case the 11×21 PFEM scheme. Then, the direction of the flow is reversed and the tracers are advected by the analytical velocity for equal time. In the absence of an analytical solution, a solution based on an adequately refined grid can be used. The difference between the final and the initial position of a tracer is a measure of the discretization effects on the trajectories. Here, the flow was advanced for two full rotations of the outer cylinder. The tracers were initially placed in the wider gap, along the line of symmetry. Representative streamlines have been plotted for reference. Figure 8 should be compared with Figure 6. The error in the neighborhood of the separation line can be anticipated from the comparison of the streamline portraits. However, the relatively large errors in the vicinity of the outer cylinder cannot be explained from the streamlines alone and should be attributed to different circulation times. The calculation of mixing patterns is expected to be affected through a similar mechanism.

Notice that in the calculations of Figures 6–8, the time integration error has been kept to a minimum. The integrations were performed using a fourth-order Runge-Kutta scheme, with the step size chosen so that the time integration errors were at least a couple of orders of magnitude lower than the discretization errors. An estimate of the time integration error was obtained by repeating the calculations with half the time step. The difference between the numerical results with the two steps were compared with the difference between the two approximate solutions and the exact one. This procedure was not presented for economy of space.

Discretization vs. time integration error

The theoretical analysis of this section revealed that the mechanisms for the evolution of the errors induced by time integration and by discretization are similar, as is evident from a comparison of Eqs. 26 and 36. In both cases, the error behaves as a material line and its growth is determined by the flow field kinematics. In addition, its magnitude depends on the accuracy of the numerical scheme.

Despite their similarities, there is at least one fundamental difference. For a given flow field, either exact or approximate, the error associated with the time integration can be controlled, using adaptive time steps and high-order methods. As a result, its magnitude can be effectively reduced to the level of the round-off error, most probably at the expense of the computational time. On the other hand, once an approximate numerical solution has been obtained, the lower limit of the error in the calculated particle trajectories is fixed. If $|\Delta x_D| \gg |\Delta x_N|$, the use of elaborate and costly time integration schemes will simply be a waste of computational time, since the overall error will be controlled by the discretization.

Given that the growth of both types of error is controlled by the flow kinematics, a comparison of their relative magnitude should be based on the relative magnitude of the associated incremental errors Δx_D and Δx_N. Once again, the assumption of a constant time step is made. For a kth-order space discretization technique and an mth-order time integration scheme $|\Delta x_D| = C_D(\Delta x_G)^{k+1}\Delta t$ and $|\Delta x_N| = C_N(\Delta t)^{m+1}$. Then, for $|\Delta x_N| \le |\Delta x_D|$, it suffices that $\Delta t \le [(C_D/C_N)(\Delta x_G)^{k+1}]^{(1/m)}$. Also, one can compare the order of the magnitude of the computational cost involved in obtaining the discretized solution and performing a time integration. Take, for example, a two-dimensional steady flow where the velocity field has been obtained using a first-order discretization scheme in the primary variable formulation (velocities and pressure) and a frontal solver for the solution of the linear problem. Assume also that the fourth-order Runge–Kutta is used for the time integration. Then, the computational cost for the solution of the discretized problem is the same as $O(10^7)$ particle trajectory calculations, if $|\Delta x_D| = |\Delta x_N| = 10^{-5}$, and $O(10^{14})$, if $|\Delta x_D| = |\Delta x_N| = 10^{-10}$. In obtaining these estimates it was assumed that the flow domain dimensions and the limits of time integration are $O(1)$ and $C_D = C_N = 1$. In time-dependent flows with a strong stretching character, such as the ones examined in the following section, it is likely that more than, say, 10^6 tracer particles may be needed for accurately representing the evolution of a material line.

Approximation Errors in Dynamical Tools

The discussion in previous sections was restricted to steady flows. In this section, the emphasis is placed on chaotic flows. Standard mixing studies employ a number of tools, such as Poincaré maps, periodic points, and experiments and simulations of dye advection. Here we are concerned with the effects of computational errors on usage of these tools.

As before, the key point is that the error behaves like a material line (Eq. 33). In chaotic flows material lines experience exponential stretching and their magnitude grows rapidly. The same can be said for the errors. In the remainder we have focused on discretization errors. The basic premise is that, as discussed in the previous section, the time integration errors are easier to control. The fourth-order Runge–Kutta method is used for the time integration. In every case, the time integration error is at least a couple of orders of magnitude lower than the discretization error.

Poincaré maps

Despite the various shortcomings of Poincaré maps as a mixing tool, they are quite useful in revealing symmetries and the existence of unmixed regions (periodic islands). In addition, since their calculation is computationally inexpensive, compared to other dynamical tools, their use is quite popular. Of special interest here is exactly how the periodic islands are modified due to the approximations in the velocity field.

Consider some representative results from the journal-bearing flow. The 180° counterrotating protocol has been chosen as a test case, since it contains two characteristic period-1 islands. In Figure 9 the Poincaré maps based on the analytical velocity field (Figure 9a), the 11×21 PFEM approximate velocity field (Figure 9b and 9c), and BIEM velocity field (Figure 9d and 9e) are compared, using the same set of initial conditions. The two islands present in Figure 9a are also present in Figure 9b, although their shape and size have been altered. A "chaotic" band (denoted B) has appeared surrounding the bigger island (A) (Figure 9a). Area B does

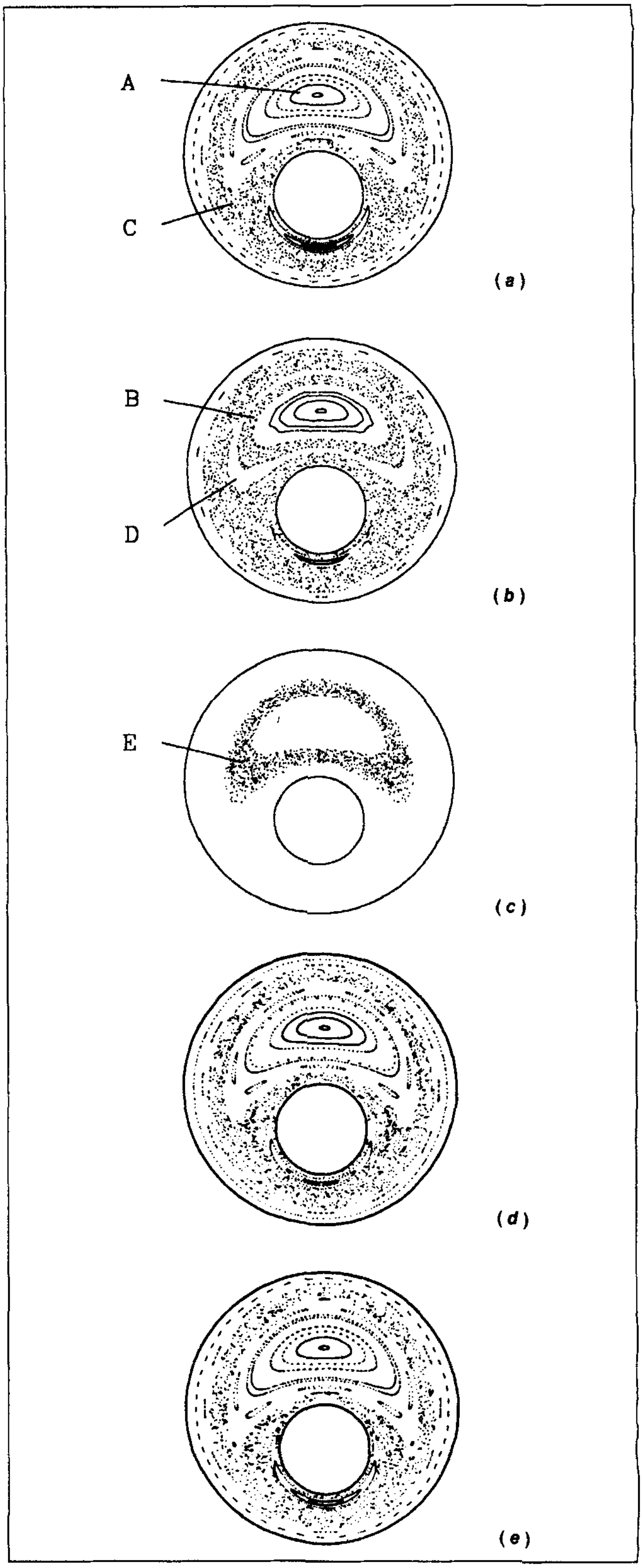

Figure 9. Time-periodic journal bearing flow ($\mu = 2$, $e = 0.45$, $\Omega = -3$).

Poincaré maps for the 180° protocol: (a) analytical velocity field; (b) 11×21 PFEM field; (c) 11×21 PFEM field; (d) BIEM field, 120 elements on outer cylinder, 40 elements on inner cylinder; and (e) BIEM field, 160 elements on outer cylinder, 80 elements on inner cylinder with different initial conditions.

not communicate with the chaotic region of the flow (C), as it is apparent from the unfilled band (D) that surrounds it. Further insight on this region is provided in Figure 9c. Starting from a different set of initial conditions, which form the short, observable line, the blurry (B) and the unfilled (D) bands of Figure 9b appear connected into a single, blurry area (E). Again, this region does not communicate with the rest of the domain. Apparently, area E is limited by a KAM-like surface. The comparison of Figures 9b and 9c suggests that even more KAM surfaces are hidden in the same area, like the surface that separates the blurry (area B) and the unfilled (area D) region of Figure 9b. Furthermore, there is also the possibility that some island chains of observable size have survived within area E (further simulations with yet another set of initial conditions, clearly identified one 10-island chain). Poincaré maps in Figure 9d and 9e, on the other hand, are more crisp and closely resemble Figure 9a. The KAM surface near the outer cylinder in Figure 9a is reproduced in Figure 9e using a more accurate velocity field (maximum and average error values are 0.0007 and 0.00015, respectively).

It can be suggested, based on a liberal interpretation of the Poincaré–Birkhoff theorem (for example, Ottino, 1989), that the chains of alternating hyperbolic–elliptic points that surround the central elliptic point, are more seriously affected. However, many KAM surfaces do survive and hinder the communication with the chaotic region (Figure 9c). (Rigorously speaking, theorems such as the KAM and the twist theorem do not apply here, since the approximate flow is not Hamiltonian, because the continuity equation is not uniformly satisfied due to various approximations. Nevertheless, the deviations from the continuity are small and the theory of Hamiltonian systems can provide some hints on the system behavior.)

Overall, small-scale features in the Poincaré map are not expected to survive, due to discretization errors. A perfunctory visual observation of such maps can lead to wrong conclusions. Indeed, it is conceivable that, with a different initial placement of the markers, area E (Figure 9c) would look connected with the chaotic region of the flow (area C), giving the impression of a single chaotic region. It should be noticed that this is a generic problem of Poincaré sections, even when an exact velocity field is available (poor communication between manifolds, slow rates of mixing, and so on).

Poincaré maps are qualitative tools. They provide a first look into the mixing flow, but their information cannot be easily quantified (for example, they do not give information regarding mixing rates). Similar difficulties apply when one attempts to quantify the error effects. Our experience suggests that a common indication of inaccuracies is the appearance of "fuzzy" boundaries; area B in Figure 9b is an exaggerated example. The existence of such areas in the actual flow can only be resolved with mesh refinement. Alternative quantitative information regarding the accuracy of the simulations can be obtained from other dynamical tools, such as material line deformations and the location of periodic points.

Individual particle trajectories in chaotic flows

It has been shown already that, in steady flows, the difference between the calculated and the exact position of a marker increases with time. What is the corresponding situation in chaotic flows?

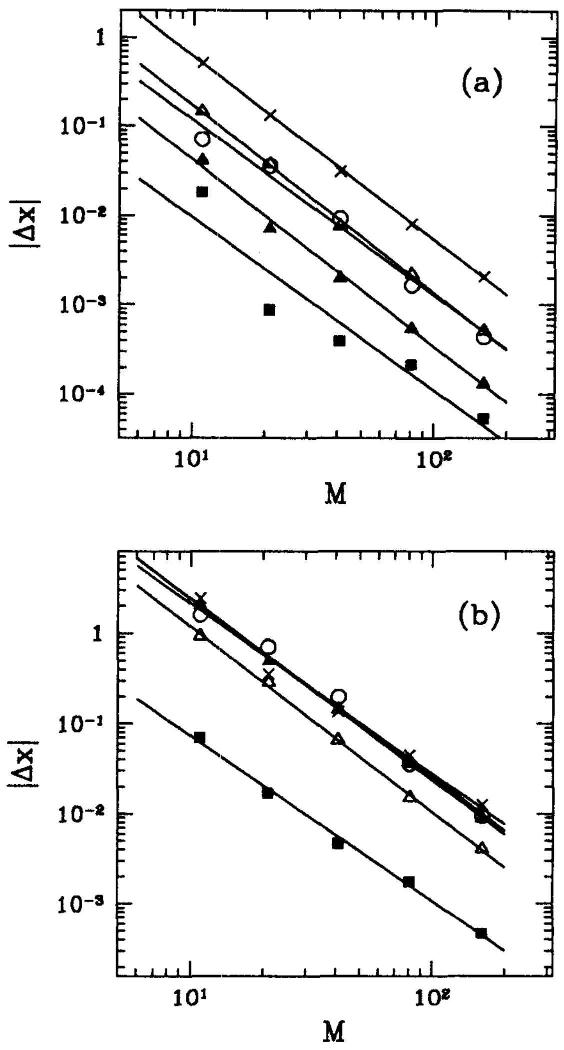

Figure 10. Time-periodic journal bearing flow ($\mu = 2$, $e = 0.45$, $\Omega = -3$), 360° protocol.

Error in the location of particles, due to velocity approximations (PFEM velocity fields of the form $M \times 2M$), as a function of M after (a) 1 and (b) 3 periods. Straight lines represent best power fit (slopes between -1.84 and -2.10). The symbols represent different initial conditions taken on the symmetry line.

A number of particles are advected for a few periods, according to approximate velocity fields and the 360° counterrotating protocol, which produces stronger stretching, compared to the 180° case. The starting locations of the particles are along the symmetry line. Grids of the form $M \times 2M$ are used to generate the approximate velocity fields.

The distance between the calculated and the exact location (error) at the end of the first and third period is plotted in Figure 10 (a and b) as a function of the number of grid points in the radial direction. The error is $O(1/M^2) = O(\Delta x_G^2)$. Note that according to Eq. 35, the incremental error, $|\Delta x_D^{(i)}|$, is proportional to $\epsilon \Delta t$. Since here $\epsilon = O(\Delta x_G^2)$, $|\Delta x_D^{(i)}|$ is proportional to $\Delta x_G^2 \Delta t$.

The magnitude of errors (161×321 PFEM grid) on the location of two particles as a function of time is presented in Figure 11. The dashed line corresponds to a particle located

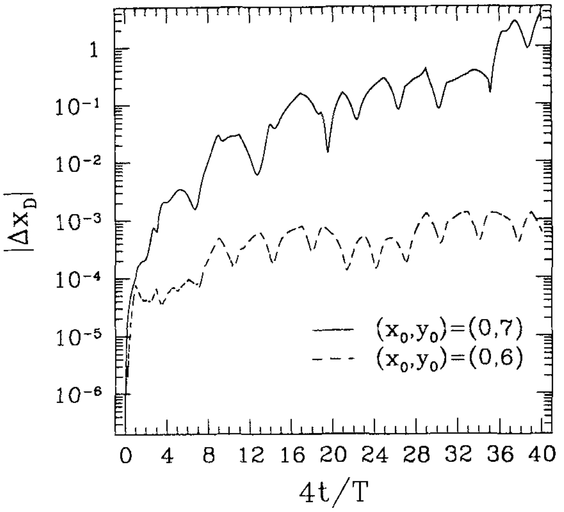

Figure 11. Time-periodic journal bearing flow (parameters as in Figure 10).

Growth of the global error (PFEM 161×321) as a function of time for a point located in the chaotic region (——) and a point located in a regular island (---).

within the period-1 island of this flow. The growth of its associated error is slower, compared to the error corresponding to a particle placed within the chaotic region (continuous line). A rough estimate based on the results of Figures 10 and 11 states that for an error below 0.1, after 10 periods, the number of grid points per side should have been of the order of 10^5.

In Figure 12, the magnitude of the error in the location of the second particle (161×321 grid) is compared to the length of two material lines with different initial orientations, starting from the same point and moving according to the analytical flow field. Due to the stretching character of the flow, the two material lines have aligned with the direction of stretching after one period. The error behaves as a material line also and it orients itself along the same direction. As a result, all these lines increase with roughly equal rates and the ratio of their lengths is almost constant. It should be noted that after a couple of periods, the addition of the incremental error, $\Delta x_D^{(i)}$, has only a minor effect on the magnitude of the error. The principal mechanism of its growth is the stretching of the flow.

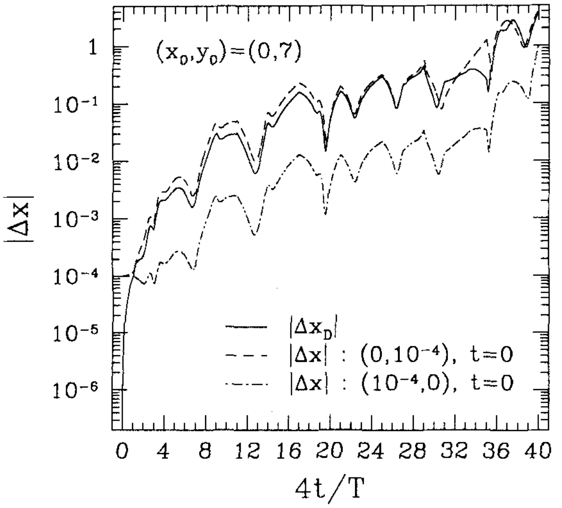

Figure 12. Time-periodic journal bearing flow (parameters as in Figure 10).

Growth of global error (PFEM 161×321) for a point within the chaotic region (——) and the length of two material lines, (--- and -·-·-), of initial length 10^{-4} located at (x_0, y_0) and aligned along the x and y axes, respectively, as a function of time.

In summary, the picture just sketched is as follows. The error in the location of a particle scales with the error in the velocity field. Since errors behave as material lines, they progressively become aligned with the local direction of the striations, and their magnitude, as a function of the time, is determined by the flow field. In chaotic flows the error increases exponentially fast. As a result, the accurate tracking of particles becomes increasingly difficult with time. It should be pointed out that traditional mesh refinement does not help much. For example, doubling the number of grid points per side will decrease the error to the one-fourth (second-order method). On the other hand, the previous level of error will be reached after, roughly, two more periods, if the length of a material line doubles with every period. Parenthetically, the use of spectral and pseudospectral methods can be slightly more advantageous in such cases, due to their exponential convergence with mesh refinement.

Fortunately, the preceding pessimistic estimates can be relaxed by using the *shadowing lemma* (Grebogi et al., 1990). Consider Eq. 3. Due to the discretization error, the relation is substituted by $x^{(i+1)} = f(x^{(i)}) \pm \Delta x$, where Δx represents the error after one period. According to this lemma, there exists an actual trajectory that "shadows" the calculated one within a distance of $\sim O(\sqrt{|\Delta x|})$ for $N \sim O(1/\sqrt{|\Delta x|})$ periods. Then, by doubling the grid points in a second-order method and, consequently, decreasing the error to one-fourth, it is expected that the calculated path will approximate a real one for double the number of periods.

Deformation of material lines

Line deformation provides important information regarding the stretching strength and the mixing abilities of a particular flow. However, following line deformation in a chaotic flow is computationally demanding. Franjione and Ottino (1987) showed that the computational time and memory requirements of such calculations soon exceed those available to most of the researchers today.

In this section we compare the deformation of material lines as predicted by the exact and the approximate velocity fields in the journal-bearing mixing flow. The question under consideration is how the particle tracking error affects the length and the small-scale structures in a mixing flow.

Figure 13a shows a straight line along the symmetry line advected for three periods using the mildly stretching 180° protocol. Most of the line lies within the chaotic region (Figure 9). The deformation of this line according to the exact flow field is shown in Figure 13a, while the coarse grid (11×21) PFEM and BIEM velocity fields have been used in Figures 13b and 13c.

The overall appearance of the deformed line has been fairly reproduced by the approximate fields. Of course, there are

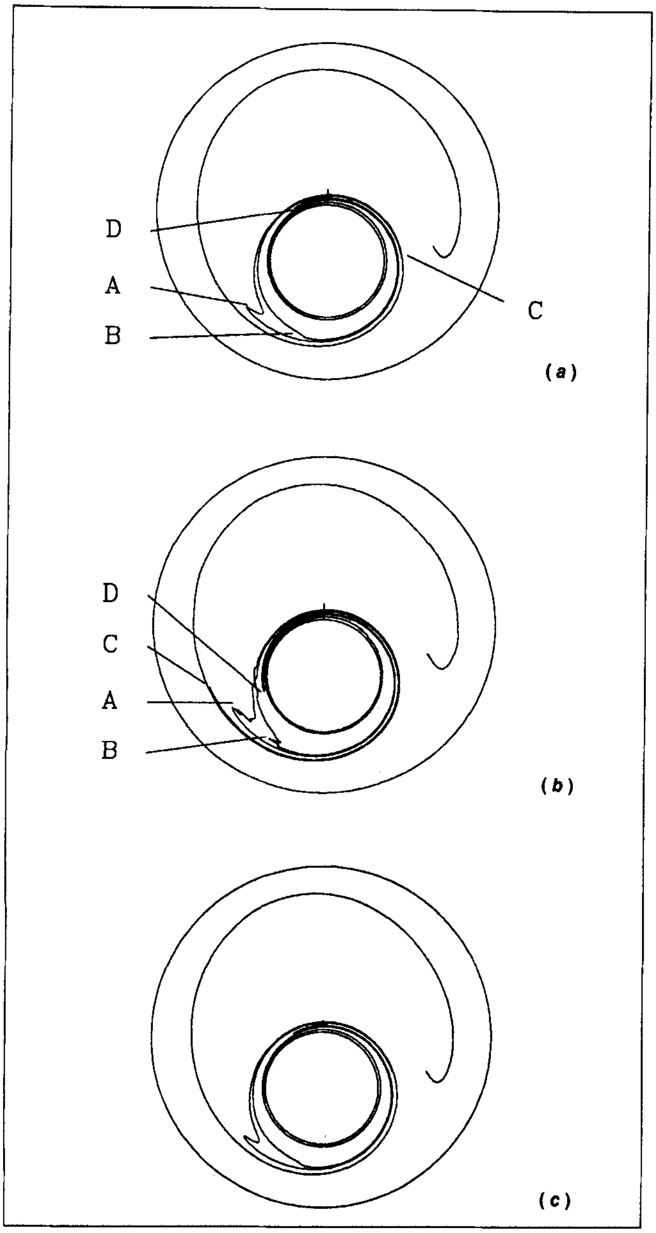

Figure 13. Time-periodic journal bearing flow (parameters as in Figure 9).

Deformation of a material line, initially located on the symmetry line and close to the inner cylinder, after 3 periods according to (a) the analytical velocity field; (b) the 11×21 PFEM field; and (c) BIEM field, 120 elements on outer cylinder, 40 elements on inner cylinder.

differences as well, most notably the jiggled texture of the approximate line around folds A and B in Figure 13b. This phenomenon may be attributed to the discontinuities in the derivatives of the discretized velocity. In any case, the locations of these two folds have not been significantly altered. More interesting is the movement of the sharper folds, C and D. For example, the fold C has come all the way to the left part of Figure 13b. Finally, a number of minor folds have appeared in the approximate field (E and F).

Despite the similarities of the deformed lines of Figures 13a and 13b, a detailed comparison reveals substantial disagreement. The error in the locations of individual particles constituting the lines of Figures 13a and 13b are compared in Figure 14. The distance between the calculated and the exact location is plotted as a function of the initial radial coordinate. For some of the particles this distance is of the order of the dimensions of the domain. However, errors in the location of individual particles orient along the local direction of stretching and are not easily detected by visual observation.

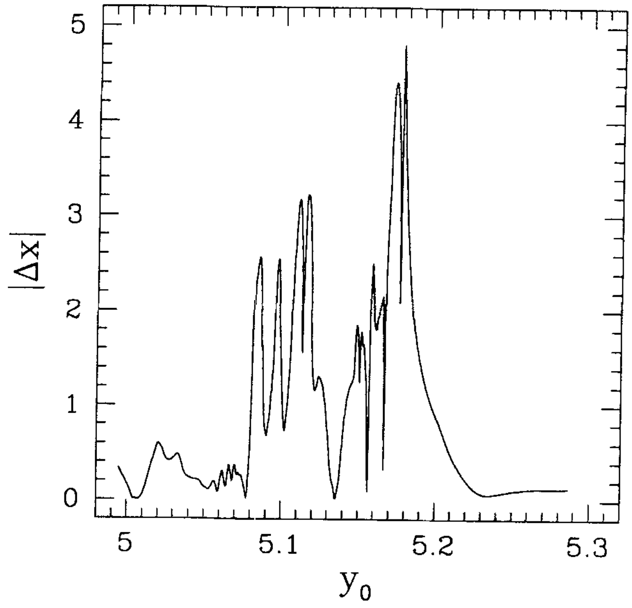

Figure 14. Error in the location of the particles of Figure 13b vs. their initial coordinate.

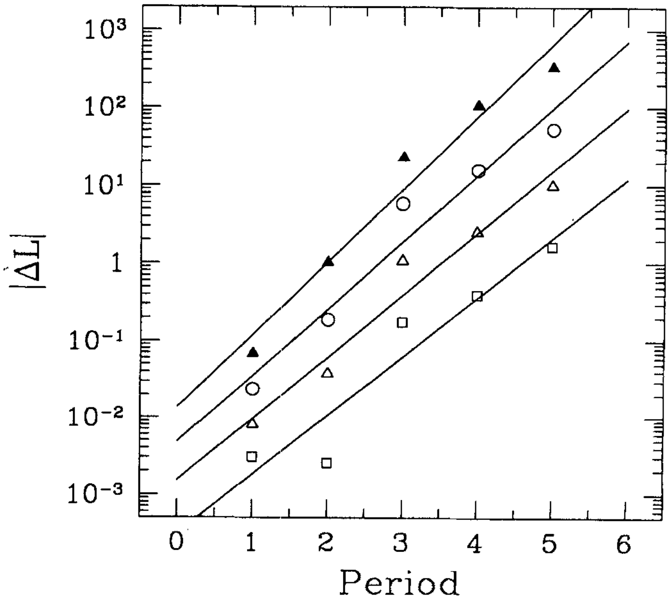

Figure 15. Time-periodic journal bearing flow (parameters as in Figure 13).

Error in the total length of a line segment initially located on the symmetry line and close to the inner cylinder as a function of the number of periods for various approximate PFEM velocity fields: (▲) 11×21; (○) 21×41; (△) 41×81; and (□) 81×161.

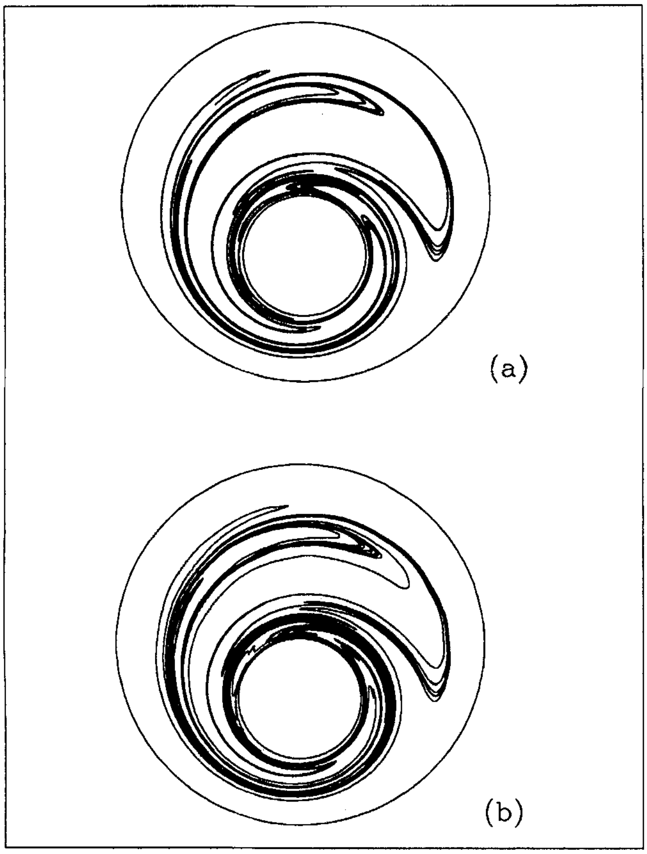

Figure 16. Time-periodic journal bearing flow (parameters as in Figure 10).

Deformation of a material line, initially located on the symmetry line and close to the inner cylinder (a) after 5 periods according to the analytical flow field, and (b) after 4 periods according to the 11×21 PFEM field.

A dramatic example is provided by Figure 13; the difference in the overall length between the two lines in (a) and (b) is more than 40%.

The error in the total length, for the different grids, has been plotted in Figure 15, as a function of the number of periods. The difference between the calculated and the exact length increases exponentially with time. The error after five periods ranges from less than 1% for the finer grid to more than 140% for the coarser one. In addition, Lyapunov exponents for the exact and the approximate velocity fields were calculated from the line-length data. The error in the value of these parameters scales roughly with Δx_G^2.

Finally, in Figure 16 longer time advection patterns (5 and 4 periods) are compared for the exact and the approximate PFEM field, using the stronger stretching, 360° protocol. Once again, the overall picture (local direction, major folds) is well reproduced by the approximate field, but the differences in the details (striation length, minor folds) are significant. In fact, after four periods the length of the deformed line according to the approximate field is more than three times the exact length.

The error in the length of a material line does provide a quantitative measure of the accuracy of the calculations. Obviously, the level of acceptable accuracy is determined from the requirements of the final application. For example, in reactive mixing, the apparent reaction rate is affected by the length of the interface area (line in two dimensions). Therefore, errors in the deformation of a material line should be minimized. However, if the objective of the simulation is to comparatively evaluate, say, the effect of a geometrical parameter on the mixing rate, wider margins of error may be acceptable.

Table 1. Location of Period-1 Points for the Time-Periodic Journal Bearing Flow ($\mu = 2$, $e = 0.45$, $\Omega = -3$), 360° Protocol, as Calculated by the Exact and Two Approximate PFEM Velocity Fields*

11×21	21×41	Exact
1.894444	*1.894444*	*1.894444*
2.360274	2.368072	2.367330
2.508546	2.501261	2.498903
2.893857	2.893588	2.893627
2.994444	*2.994444*	*2.994444*
4.994444	*4.994444*	*4.994444*
5.205583	5.211168	5.212781
5.316550	5.315743	5.315509
6.051239	6.049452	6.049988
7.894444	*7.894444*	*7.894444*

*Only the y-coordinate is given (see Figure 2) since all points are located on the symmetry line (small gap $1.894444 \le y \le 2.94444$, large gap $4.994444 \le y \le 7.894444$). Italics denote periodic points on the boundary surface (predicted exactly by the approximate fields).

Periodic points

Periodic points can be quite helpful in analyzing the mixing character of a flow (Jana et al., 1994). Their stability to perturbations of the mixing protocol identifies possible optimum mixing conditions; the eigenvalues of hyperbolic points give a good indication of the local stretching rate as well as the local direction of striations. It has been already shown that crude approximations of a velocity field—resulting in substantial errors in the location of an individual particle—do not translate into large errors in the local direction of the striations. It was suggested that this is a consequence of the alignment of the error with the direction of stretching. An implicit assumption in this statement is that the local direction of stretching is not overly affected by the approximations in the velocity field. Since periodic points control the local stretching, the effect of the discretization on these points is examined here.

To start with notice that, due to the symmetry of the prototype flow under consideration, period-1 points always fall on the symmetry line. Higher period points appear in chains and are arranged symmetrically. As a result, the search for periodic points is simplified. This is also true for the approximate flow, since the discretization used here preserves the symmetry of the flow. The location of the period-1 points for the 360° protocol calculated with two discretized and the analytical velocity field are shown in Table 1. The points are denoted by their y-coordinate in the Cartesian system. Except for the period-1 points on the boundaries of the flow domain (shown in italics), for which their exact location is predicted, the error in the location of these points scales with Δx_G^2, similar to the error of the velocities. For higher-order periodic points, the error is higher. Moreover, new chains of periodic points may appear, but vanish with mesh refinement.

Table 2. Error in the Location of the Hyperbolic Points of Table 1 Compared to the Predictions of Eq. 40

y-Coord.	Eigenvalue	11×21		21×41		41×81	
(Exact Velocity)		Predicted	Actual	Predicted	Actual	Predicted	Actual
5.3155	36.3047	1.23×10^{-3}	1.04×10^{-3}	2.45×10^{-4}	2.34×10^{-4}	5.39×10^{-5}	5.37×10^{-5}
2.3673	31.3211	2.94×10^{-3}	7.06×10^{-3}	7.48×10^{-4}	7.42×10^{-4}	1.86×10^{-4}	1.86×10^{-4}
2.8936	13.7183	3.33×10^{-4}	2.30×10^{-4}	4.41×10^{-5}	3.90×10^{-5}	2.52×10^{-5}	2.43×10^{-5}
2.4989	8.0514	1.01×10^{-2}	9.64×10^{-3}	2.45×10^{-3}	2.36×10^{-3}	5.90×10^{-4}	5.90×10^{-4}
5.2128	2.5280	1.79×10^{-2}	7.20×10^{-3}	1.84×10^{-3}	1.61×10^{-3}	4.75×10^{-4}	4.21×10^{-4}

It is interesting that the error in the location of the periodic points (Table 1) is very small compared to the errors in the location of individual particles. A linearized analysis is used below to explain this behavior.

The movement of a particle within a period can be represented by the map $f(\boldsymbol{x};\epsilon)$ where ϵ describes the perturbation due to the approximation. For the exact flow field, $\epsilon = 0$. The mapping (Eq. 4) in the vicinity of a periodic point, $\boldsymbol{x}_0$, can be expanded as

$$\boldsymbol{x}^0 + \Delta \boldsymbol{x} = \boldsymbol{f}^1(\boldsymbol{x}^0 + \Delta \boldsymbol{X};\epsilon) = \boldsymbol{x}^0 + \boldsymbol{F}\cdot\Delta \boldsymbol{X} + \epsilon\frac{\partial \boldsymbol{f}^1}{\partial \epsilon}, \quad (38)$$

with $\boldsymbol{F}$ being the deformation matrix at $\boldsymbol{x}^0$. The last term in the righthand side of Eq. 38 indicates where a particle, which is initially placed at the exact location of the periodic point, will end up due to the approximate flow and will be denoted $-\boldsymbol{b}^\epsilon$. Its magnitude is a local measure of the error in the location of a particle after one period, due to the velocity approximation. According to Eq. 38, the location of the new periodic point, for the ϵ-perturbed flow, $\boldsymbol{x}^0 + \delta\boldsymbol{x}^\epsilon$, satisfies the equation

$$\boldsymbol{x}^0 + \delta\boldsymbol{x}^\epsilon = \boldsymbol{x}^0 + \boldsymbol{F}\cdot\delta\boldsymbol{x}^\epsilon - \boldsymbol{b}^\epsilon. \quad (39)$$

Then

$$(\boldsymbol{F} - \boldsymbol{I})\cdot\delta\boldsymbol{x}^\epsilon = \boldsymbol{b}^\epsilon. \quad (40)$$

For a hyperbolic point in a two-dimensional flow, the eigenvalues of $\boldsymbol{F}$ are, l and $1/l$. Matrix $\boldsymbol{F}$ is completely defined, up to rotation, from l and the angle, θ, between its two eigendirections. If the x-coordinate is oriented along the direction of the eigenvector with magnitude l, then

$$\boldsymbol{F} = \begin{bmatrix} l & \dfrac{1-l^2}{l}\tan\theta \\ 0 & \dfrac{1}{l} \end{bmatrix}. \quad (41)$$

From Eq. 40, one can obtain the ratio $|\delta\boldsymbol{x}^\epsilon|/|\boldsymbol{b}^\epsilon|$ as a function of l, θ, and ϕ, with ϕ being the orientation of $\boldsymbol{b}^\epsilon$. The matrix $(\boldsymbol{F}-\boldsymbol{I})$ is singular when l goes to 1. In this case, $|\delta\boldsymbol{x}^\epsilon|/|\boldsymbol{b}^\epsilon|$ goes to infinity, proportionally to $1/(l-1)$. On the other hand, $|\delta\boldsymbol{x}^\epsilon|/|\boldsymbol{b}^\epsilon|$ tends to a value that depends on θ and ϕ, when l goes to infinity. For constant θ, the maximum occurs when $\phi = \pi/2$ and it is equal to $1/\cos(\theta)$. Notice that a large value of $|\delta\boldsymbol{x}^\epsilon|/|\boldsymbol{b}^\epsilon|$ indicates a large change in the location of the periodic point and significant local variations of the mixing patterns.

For a symmetric flow, like the one under consideration, $\delta\boldsymbol{x}^\epsilon$ is oriented along the symmetry line. In the local coordinate system described earlier, it forms an angle $\theta/2$, or $(\theta+\pi)/2$ with the eigenvector corresponding to l. As l goes to 1, $|\delta\boldsymbol{x}^\epsilon|/|\boldsymbol{b}^\epsilon|$ goes to infinity, proportionally to $1/(l-1)$. On the other hand, when l goes to infinity, $|\delta\boldsymbol{x}^\epsilon|/|\boldsymbol{b}^\epsilon|$ tends to zero, as $1/l$. Therefore, the location of a hyperbolic point with a high stretching rate will be hardly affected due to the perturbation, while the opposite will happen to a parabolic point $(l=1)$.

Note that in the preceding analysis, $\boldsymbol{b}^\epsilon$ has been left undetermined. Indeed, it is a complicated function of the trajectory of a particle and the distribution of errors within the flow field and, consequently, it can be affected by the distribution of gridpoints within the domain. In general, its value is expected to scale with the error in the velocity field.

The predictions of Eq. 40 were compared to actual findings for the 360° protocol. Values of l and θ were calculated for the hyperbolic points of Table 1. Then, the magnitude of $\boldsymbol{b}^\epsilon$'s was numerically estimated for every point and each discretization. The predicted $|\delta\boldsymbol{x}^\epsilon|$'s are finally compared with the actual $|\delta\boldsymbol{x}^\epsilon|$. This comparison is summarized in Table 2. The agreement between the predicted and the actual values is very good, especially for the finer mesh.

Notice that the preceding analysis is not limited to perturbations due to flow field approximations, but also describes perturbations due to changes in the flow-controlling parameters (such as the protocol).

Conclusions

Simulations are inherently subject to approximation errors. Therefore, their successful utilization relies heavily on the understanding and control of such errors. Mixing simulations, in particular, are more susceptible to approximation errors simply due to the mere size of the computational load, which inevitably leads to simplifications or compromises regarding the accuracy of the simulations. Due to inaccuracies caused by the discretization the numerical integration and the finite accuracy of any computational device, calculated particle trajectories are only approximations of the actual ones. The error, defined as the distance between the exact and the calculated particle location, behaves as a differential material line. It is deformed by the flow field and its length, on the average, grows with time.

Discretization and time integration approximations affect the particle location through a similar mechanism. In both cases, an incremental error is introduced at every time step. Its magnitude is controlled by the accuracy of the numerical technique, which, in turn, is controlled by the grid size or the time step, respectively. The cumulative or global error, at any given time, is the sum of all the previously introduced errors as they have grown within the flow field. In addition, the error aligns with the stretching direction.

In steady, two-dimensional and bounded flows, the overall or global error increases proportionally with at most the square of the elapsed time on the average, although the details of the particular flow and the time integration scheme influence the short and long time global error behavior. Simple visual examination of the streamline portrait is not sufficient for the evaluation of the quality of a computed velocity field, because the error tends to align with the direction of the streamlines. Consequently, its component along this direction is larger and translates into an error in the circulation time. In particular, when the flow field is symmetric, the streamlines produced by the computed velocity field always close or end on the boundary, irrespective of whether the velocity field satisfies the continuity equation or not. A possible exception to this rule are streamlines that do not cross the symmetry line.

In chaotic flows, errors increase in a qualitatively similar manner, although the growth is much faster due to the exponential stretching. Very quickly, their magnitude becomes of the order of the dimensions of the domain. Despite this behavior, a distinguishing characteristic of chaotic systems, it was found that the deformation of a material line is captured satisfactorily, in qualitative terms, even when relatively inaccurate velocity fields, with Euclidean error of up to 5%, are used. This phenomenon can be explained once again in terms of the tendency of the error to align with the manifolds of the hyperbolic points. Furthermore, it was proved that the error in the location of hyperbolic points due to velocity approximations is lower for points with high eigenvalues. Hyperbolic points and their associated manifolds are usually the ones mostly responsible for the mixing patterns in the chaotic regions. However, approximate velocity fields generate chains of fictitious periodic points, usually of higher order. In Poincaré maps, approximation errors modify the boundaries of regular islands. Their primary effect is the breaking of KAM surfaces into chains of high-order islands. Consequently, the boundaries of regular islands become hazy or, occasionally, appear to belong to the chaotic region and as a result, the well-mixed area appears to cover a larger portion of the domain. More importantly, it should be noted that, even when the qualitative picture is fairly well approximated, quantitative information may not be reliable. For example, in a typical case of the material line deformation, the 5% error in the velocity field caused errors of about 150% in the length of a line.

In most real mixing problems—as opposed to this article—there is no exact reference case to compare with. Nevertheless, the body of work presented in this article suggests that the accuracy requirements for the velocity field are not as strict as the exponential stretching of chaotic flows seems to suggest, especially if only a qualitative description of the mixing patterns is needed. For example, the 21×41 PFEM velocity field, with about 1% maximum error seems to provide a satisfactory sketch of the mixing patterns of the 180° protocol. Yet, considerable caution should be exercised when quantitative information is sought (such as length of a material line as a function of time or stretching rate distributions). In such cases, standard numerical analysis tools, such as mesh refinement, become mandatory. Without such tests, results of numerically generated mixing calculations are, at best, suspect.

Acknowledgment

This work was supported by DOE, Division of Basic Energy Sciences.

Notation

C = constant
I = identity matrix
O = order of
Δx_R = local error (vector) due to round-off
Δx_N = local error (vector) due to discretization
δ_{ij} = Kronecker delta function
δx^{ϵ} = error in the location of a periodic point due to velocity approximations
μ = dimensionless gap (concentric and eccentric cylinders)

Subscripts and Superscripts

0 = initial condition
D = calculated quantity due to discretization error
i, j = coordinates (x, y for Cartesian system and r, θ for cylindrical system)
N = calculated quantity due to time integration error
· = time derivative
(i) = quantity corresponding to the ith time step

Literature Cited

Avalosse, T., M. Crochet, A. Fobelets, and C. Dehennau, "Numerical Simulation of Mixing," *Proc. Cong. on Rheology*, Vol. 1, P. Moldenaers and R. Keunings, eds., Brussels, Belgium, p. 318 (1992).

Candy, J., and W. Rozmus, "A Symplectic Integration Algorithm for Separable Hamiltonian Functions," *J. Comput. Phys.*, **92**, 230 (1991).

Chaiken, J., R. Chevray, M. Tabor, and Q. M. Tan, "Experimental Study of Lagrangian Turbulence in a Stokes Flow," *Proc. R. Soc. Lond. A*, **408**, 165 (1986).

Channell, P. J., and C. Scovel, "Symplectic Integration of Hamiltonian Systems," *Nonlinearity*, **3**, 231 (1990).

Franjione, J. G., "Development and Application of Techniques for the Analysis of Chaotic Mixing in Two- and Three-Dimensional Flows," PhD Diss., Univ. of Massachusetts, Amherst (1991).

Franjione, J. G., and J. M. Ottino, "Feasibility of Numerical Tracking of Material Lines and Surfaces in Chaotic Flows," *Phys. Fluids*, **30**, 3641 (1987).

Grebogi, C., S. M. Hammel, J. A. Yorke, and T. Sauer, "Shadowing of Physical Trajectories in Chaotic Dynamics: Containment and Refinement," *Phys. Rev. Lett.*, **65**, 1527 (1990).

Jana, S. C., G. Metcalfe, and J. M. Ottino, "Experimental and Computational Studies of Mixing in Complex Stokes Flows: The Vortex Mixing Flow and Multicellular Cavity Flows," *J. Fluid Mech.*, **269**, 199 (1994).

Jana, S. C., and J. M. Ottino, "Chaos-Enhanced Transport in Cellular Flows," *Phil. Trans. R. Soc. Lond.*, **A338**, 519 (1992).

Niederkorn, T. C., and J. M. Ottino, "Mixing of Viscoelastic Fluids in Time-Periodic Flows," *J. Fluid Mech.*, **256**, 243 (1993).

Ottino, J. M., *The Kinematics of Mixing: Stretching, Chaos, and Transport*, Cambridge Univ. Press, New York (1989).

Pozrikidis, C., *Boundary Integral and Singularity Methods for Linearized Viscous Flow*, Cambridge Univ. Press, Cambridge (1992).

Swanson, P. D., "Regular and Chaotic Mixing of Viscous Fluids in Eccentric Rotating Cylinders," PhD Thesis, Univ. of Massachusetts, Amherst (1991).

Swanson, P. D., and J. M. Ottino, "A Comparative Computational and Experimental Study of Chaotic Mixing of Viscous Fluids," *J. Fluid Mech.*, **213**, 227 (1990).

Tanguy, P. A., R. Lacroix, F. Bertrand, L. Choplin, and E. Brito De La Fuente, "Finite Element Analysis of Viscous Mixing with Helical Ribbon-Screw Impeller," *AIChE J.*, **38**, 939 (1992).

Tjahjadi, M., and J. M. Ottino, "Stretching and Breakup of Droplets in Chaotic Flows," *J. Fluid Mech.*, **232**, 191 (1991).

Wannier, G. H., "A Contribution to the Hydrodynamics of Lubrication," *Quart. Appl. Math.*, **8**, 1 (1950).

Yee, H. C., P. K. Sweby, and D. F. Griffiths, "Dynamical Approach Study of Spurious Steady Numerical Solutions of Nonlinear Differential Equations: I. The Dynamics of Time Discretization and Its Implications for Algorithm Development in Computational Fluid Mechanics," *J. Comput. Phys.*, **97**, 249 (1991).

Appendix: Proof That Symmetric "Flows" Produce Close Streamlines

Consider a 2-D, symmetric domain and a 2-D symmetric vector field, $\boldsymbol{u}(\boldsymbol{x})$, that does not necessarily satisfy the continuity condition. In addition, $\boldsymbol{u}(\boldsymbol{x})$ is continuous, but its derivatives are continuous locally only (within an element). Such a field can be produced by a numerical solution of the flow equations in a symmetric flow geometry, with the additional constraint that the discretized system preserves the symmetry of the geometry. For convenience, the line of symmetry coincides with the y-axis. Then

$$u_x(x,y)=u_x(-x,y);\quad u_y(x,y)=-u_y(-x,y). \tag{A1}$$

We are interested in trajectories generated by

$$\dot{\boldsymbol{x}}=\boldsymbol{u}(\boldsymbol{x});\quad \nabla\cdot\boldsymbol{u}\neq 0. \tag{A2}$$

A "flow" function can be defined so that

$$(x,y)=\Phi(x_0,y_0;t), \tag{A3}$$

denoting that a particle located at (x_0,y_0) moves to (x,y) after time t. For a time-independent field motions can be composed (Franjione, 1991). Then

$$\Phi(x_0,y_0;t_1+t_2)=\Phi[\Phi(x_0,y_0;t_1);t_2]. \tag{A4}$$

One can define the inverse flow function

$$(x_0,y_0)=\Phi^{-1}(x,y;t), \tag{A5}$$

which coincides with the "flow" function for $\boldsymbol{u}'(\boldsymbol{x})=-\boldsymbol{u}(\boldsymbol{x})$. Then, using symmetry arguments

$$\begin{aligned}\Phi_x(-x,y;t)&=-\Phi_x^{-1}(x,y;t)=-x_0;\\ \Phi_y(-x,y;t)&=\Phi_y^{-1}(x,y;t)=y_0.\end{aligned} \tag{A6}$$

Consider then a trajectory originating from a point on the symmetry line, at $(0,y_1)$, that crosses the symmetry line again after time $T/2$, at $(0,y_2)$. Then, from Eqs. A3 and A6 one can write that

$$\begin{aligned}(0,y_2)&=\Phi(0,y_1;T/2);\\ (0,y_1)&=(-0,y_1)=\Phi(-0,y_2;T/2)=\Phi(0,y_2;T/2).\end{aligned} \tag{A7}$$

Then

$$\Phi(0,y_1;T)=\Phi[\Phi(0,y_1;T/2);T/2]=\Phi(0,y_1;T/2)=(0,y_1). \tag{A8}$$

Consequently, any trajectory that starts from the line of symmetry (and does not end on the boundary) returns to the same point (closed). A trajectory that starts anywhere in the domain and crosses the symmetry line (and does not end on the boundary) is also closed. It can also be shown, although it is not covered by the previous discussion, that separation streamlines are also symmetric.

Notice that this proof does not cover the cases of trajectories that do not cross the symmetry line (such as Moffat vortices in the square cavity). Furthermore, it has been assumed that the trajectory does not encounter any parabolic point.

Manuscript received Mar. 23, 1994, and revision received Sept. 23, 1994.